Journal of Sound and Vibration 330 (2011) 1121–1140

Contents lists available at ScienceDirect

Journal of Sound and Vibration

journal homepage: www.elsevier.com/locate/jsvi

Flexural vibration patterning using an array of actuators

Eyal Setter, Izhak Bucher*

Technion, Israel Institute of Technology, Faculty of Mechanical Engineering, Technion, Haifa 32000, Israel

ARTICLE INFO

Article history:
Received 1 November 2009
Received in revised form
5 July 2010
Accepted 25 September 2010
Handling Editor: A.V. Metrikine
Available online 23 October 2010

ABSTRACT

This paper describes a method to create unique vibration patterns by means of an array of actuators acting on the boundaries of the controlled structure. The method builds, in an iterative process, a black-box model by employing a series of probing external excitation vectors. Once a model has been identified, an optimization stage seeks the dynamic force-vector that generates the best approximation for a specified deformation pattern. Among the obtainable periodic responses are standing or travelling flexural waves of single or multi-frequencies in one or two spatial dimensions, as well as rotating, vortex-like, flexural waves in 2D. The paper describes the force-tuning process through which dozens of actuators can be modified automatically until the response, measured at hundreds of sensed locations, complies with the anticipated response. The excitation that yields the desired response is calculated using an over-determined set of least-squares equations that approximates the inverse of the identified model. The precise iterative tuning process can overcome some nonlinearity, manifested by additional harmonics in the response, by injecting forces that nullify their effect. Methods for wavelength optimization and wave identification in 1D and 2D are also discussed. The proposed tuning method showed good results in numerical simulation and in real world experiments.

1. Introduction

Shaping the vibration pattern of a given finite, continuous structure using external forces can be useful in several cases. For example, one desired vibration pattern is a travelling flexural wave of predetermined wavelength, amplitude, direction, and phase. Such a pattern is often used to generate propulsion, as in squeeze-film levitation and transportation devices [1,2], where a travelling pressure wave carries a levitated object. In robotics, snake-like structures make use of travelling wave movements for propulsion over solid surfaces [3], or in steering and maneuvering in a viscous fluid environment [4]. Travelling waves are also used to absorb incoming vibration in robotic arms [5]. An active vibration control method dealing with waves is investigated in [6,7] with implementation on a flexible beam and a flexible plate, respectively. The control aims to eliminate vibration modes by cancelling reflected or transmitted waves. While [5–7] aim to suppress undesired vibration, the current paper suggests a method to excite desired structural responses, such as travelling waves, while constructing a non-modal, measurements-based system model. Ultrasonic motors are a relatively recent and unique application that makes use of high frequency, short wavelength travelling flexural waves to achieve accurate and relatively high torque positioning without the need for reduction gears [8,9]. In micro-electro-mechanical systems (MEMS) applications, non-circular structures are preferable in batch micro-machining of silicon. In such application, the need arises

* Corresponding author. Tel.: +972 4 8293153; fax: +972 4 8295711.
E-mail address: bucher@technion.ac.il (I. Bucher).

0022-460X/$ - see front matter © 2010 Elsevier Ltd. All rights reserved.
doi:10.1016/j.jsv.2010.09.027

to generate rotating flexural waves in a rectangular plate that performs as the stator of a micro-ultrasonic motor. Such waves have been generated in square micro-plates by dual- or multimode excitation [10]. A similar approach to creating travelling waves in rectangular structures using single-phase actuation was introduced in [11]. For a theoretical derivation of a circumferential force distribution that yields travelling waves in one- and two-dimensional structures by means of infinite modal summation, see [12]. Another example of motion tuning is the use of rigidly oscillating plates that slide and orient parts on assembly lines by friction-induced velocity or force fields [13]. In this example, the rigid plate has six degrees of freedom and is controlled by six actuators. In other cases, elastic stretching platforms are used in growing in-vitro human heart tissues to better simulate their natural habitat and hence improve functionality of the artificially grown cells [14]. Vortex structural and acoustic power flows were analyzed by Tanaka et al. [15] for simply supported thin elastic plate under feed-forward vibration control. The vortexes, described as interference between modes of vibration were observed when two modes of vibration were affected. The method proposed in the present work allows an extended freedom in determining the vortex geometry (wavelengths, frequency, and location) but, clearly the method in [15] would yield larger amplitudes of vibration under fixed excitation level due to the proximity of the excitation frequencies to resonance. The present method is broader in scope due to its ability to tune arbitrary vibration patterns, for a predetermined set of actuators distributed only around the boundaries. The present method contrary to [14] uses a model that does not rely on specific vibration modes, under the assumption that multiple modes of vibration can play a significant role when attempting to generate a propagating phenomenon [12].

Nevertheless, to the best of our knowledge, no studies have yet considered the tuning of a given elastic structure's response in a variety of vibration patterns, including standing, travelling, single or multi-frequencies waves in one or two spatial dimensions, and rotating waves in 2D. In the current study, multi-input multi-output (MIMO) tuning experiments are conducted, with as many as 32 actuators and over 500 sensed locations (in tuning out-of-plane vibration experimentally on a membrane). The proposed method is based on extending the procedure presented in [16] to a non-square system having a large number of sensors and actuators. Furthermore, in contrast to [16], which essentially controlled a single node on a shaft, the present study is employed to experimentally control the steady-state vibrations of an entire region on a structure.

The following section describes the problem and the proposed method. The basic approach and the underlying stages are outlined in Section 2.1, followed by the mathematical description of a typical desired response in Section 2.2. Handling nonlinearities is referred to in Section 2.3, and the determination of the optimal wavelength is explained in Section 2.4. Wave identification methods are reviewed in Section 2.5. Numerical and experimental results come next. The experiment layout is presented in Section 3.1. Simulated and experimental results of 1D string and 2D membrane models are given in Sections 3.2 and 3.3, respectively. The paper ends with concluding notes in Section 4, where the merits of the proposed method are outlined.

2. Model identification and inversion

This section outlines the mathematical foundation of the proposed tuning method. The tuning process, as illustrated in Fig. 1, begins with system identification. Next, the optimal wavelength for a given excitation frequency is found, and given

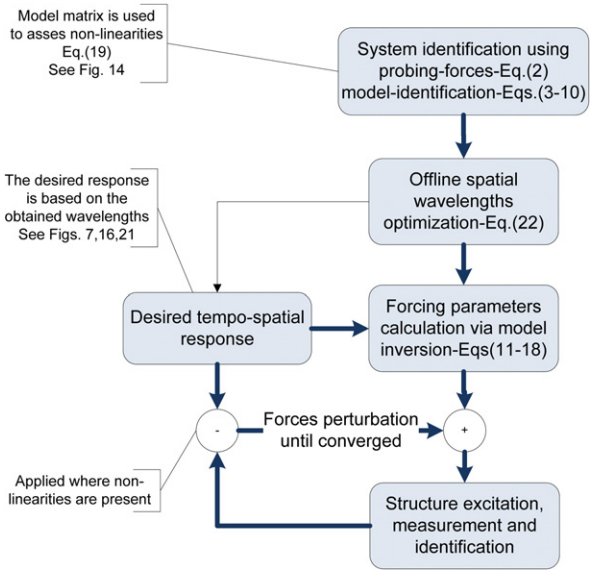

Fig. 1. The proposed tuning method scheme.

the system model, the excitation needed to yield the desired response is calculated. When the device under test exhibits a mild nonlinearity, additional perturbations are added to an extended model allowing for multi-frequency tuning that eliminate parasitic harmonics. The section ends with a short description of wave identification methods. It should be noted that Sections 2.1, 2.3 and 2.5 include previous works, which set the ground for the introduction of the newly developed concepts as given in Sections 2.2 and 2.4, and for the analysis of the results in Section 3.

2.1. Method in brief

The proposed method is based on a procedure presented in [16]. The following discussion briefly reviews this procedure and further develops it for real-world multi-output multi-input (MIMO) systems and various vibration patterns based upon new interpretations and physical findings. The proposed method aims to find the excitation parameters under which a desired structural response in terms of a specified spatial vibration pattern, e.g., travelling flexural waves is obtained. The method uses only measured response data with almost no previous knowledge of the system at hand. The sensors and actuators should be placed at suitable locations. If they are not, the proposed method can detect any deficiency or inferior deployment of the transducers. By means of the proposed enhancements, the algorithm can find the best achievable response within a family of desired patterns (e.g. travelling waves).

The proposed method will be regarded in this text as means of tuning flexural (transverse) steady state, out of plane displacements of string and membrane models. Fig. 2(a) depicts an example of an abstract structure (a membrane) excited by several actuators. The flexural vibration (out of plane displacement) is measured at certain points for a random set of orthonormal excitation vectors. Fig. 2(b) shows the same structure after the tuning process, where the structure is experiencing the desired vibration pattern.

Let us consider a system with $\mathcal{N}$ measured points and $\mathcal{M}$ exciters. The theoretical system can be described in a spatially discrete fashion (e.g., finite element—FE derived model):

$$\mathbf{M}\ddot{\boldsymbol{\eta}}+\mathbf{C}\dot{\boldsymbol{\eta}}+\mathbf{K}\boldsymbol{\eta}=\mathbf{B}\boldsymbol{\gamma}(\boldsymbol{\eta},t),\quad \boldsymbol{\eta}\in\mathbb{R}^{\mathcal{N}\times 1},\quad \boldsymbol{\gamma}\in\mathbb{R}^{\mathcal{M}\times 1},\quad \mathbf{M},\mathbf{C},\mathbf{K}\in\mathbb{R}^{\mathcal{N}\times\mathcal{N}},\quad \mathbf{B}\in\mathbb{R}^{\mathcal{N}\times\mathcal{M}}, \tag{1}$$

where $\boldsymbol{\eta}$ is the state vector of generalized coordinates representing the structural deformations, and $\boldsymbol{\gamma}(\boldsymbol{\eta},t)=\boldsymbol{\gamma}_0(t)+\boldsymbol{\gamma}_1(\boldsymbol{\eta},t)$ is the time-dependent input vector or the excitation, containing the directly influenced part $\boldsymbol{\gamma}_0(t)$, and some mild nonlinearities $\boldsymbol{\gamma}_1(\boldsymbol{\eta},t)$ that are state-vector dependent. $\mathbf{M}$, $\mathbf{C}$, $\mathbf{K}$ are the mass, damping, and stiffness matrices, respectively, and $\mathbf{B}$ is a matrix of force distribution weighting, mapping the excitation vector to the appropriate degrees of freedom.

The proposed method adapts the external excitation vector $\boldsymbol{\gamma}_0(t)$ to obtain a desired response pattern manifested by $\boldsymbol{\eta}$ in Eq. (1). The current paper focuses on steady-state time periodic vibrations, but not necessarily on pure sinusoids. The assumption of steady-state time periodic vibrations converts the differential equation (Eq. (1)) into a system of algebraic equations. The force adaptation process begins with a black-box model identification stage. In this stage, a set of independent excitation vectors is generated, the corresponding response vectors are measured, and thus the model is formed.

For a perfectly linear system, running all the exciters at the same frequency, ω_0, yields two types of distinguishing parameters per exciter—amplitude and phase. A frequency index h must be added to achieve a multi-frequency response, or if nonlinear super- and sub-harmonics are expected. The mth exciter induces a force comprised of several harmonics, i.e.

$$q_m=\sum_{h=1}^{\mathcal{P}} q_m^h,\quad m=1,2,\ldots,\mathcal{M}, \tag{2}$$

where $q_m^h=Q_m^h\cos(h\omega_0 t)+R_m^h\sin(h\omega_0 t),\quad h=1,2,\ldots,\mathcal{P}.$

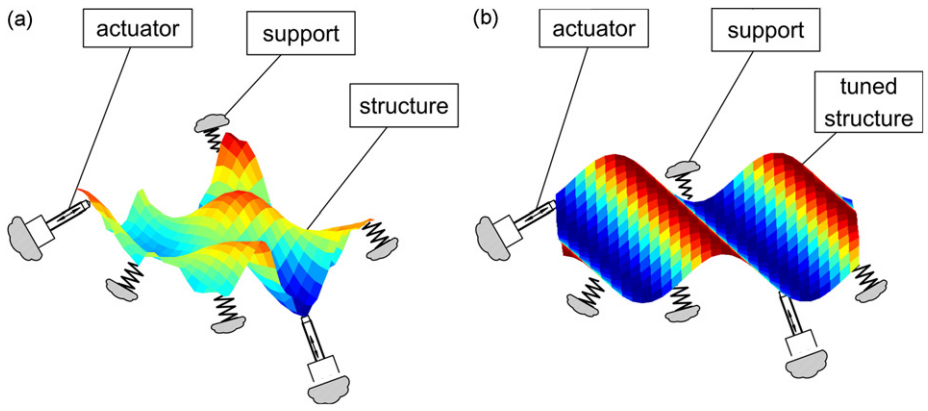

Fig. 2. (a) Vibrating structure at some $t=t_0$, before tuning the response and (b) same structure experiencing tuned vibration of a travelling flexural wave at $t=t_1$.

Here $|Q_m^h + iR_m^h|$, $(\mathrm{i} \equiv \sqrt{-1})$ represents the force amplitude at the mth excitation point. This component has excitation frequency $h\omega_0$ (rad/s), and its phase is dictated by $\arg(Q_m^h + \mathrm{i}R_m^h)$ relative to a common reference. Hence, Q_m^h,R_m^h are tunable parameters.

For the model identification stage, $\mathcal{M}$ exciters require an excitation basis of $2\mathcal{M} \times 2\mathcal{M}$ parameters per frequency. Accordingly, the system's measured response at the nth point ($n = 1,2,\ldots,\mathcal{N}$) to the rth ($r = 1,2,\ldots,2\mathcal{M}$) excitation vector of the hth frequency component is

$$a_{r,n}^h = A_{r,n}^h \cos(h\boldsymbol{\omega}_0 t) + B_{r,n}^h \sin(h\boldsymbol{\omega}_0 t). \tag{3}$$

The force amplitude of the mth exciter of the rth excitation vector of the hth frequency component is

$$q_{r,m}^h = Q_{r,m}^h \cos(h\boldsymbol{\omega}_0 t) + R_{r,m}^h \sin(h\boldsymbol{\omega}_0 t). \tag{4}$$

When Eqs. (3) and (4) are combined for the entire system and rearranged by the coefficients of $\cos(h\omega_0 t)$, $\sin(h\omega_0 t)$, the result is the following set of equations per frequency component (for a single harmonic index h):

$$\begin{pmatrix} A_{r,1} \\ \vdots \\ A_{r,\mathcal{N}} \\ B_{r,1} \\ \vdots \\ B_{r,\mathcal{N}} \end{pmatrix} = \begin{pmatrix} H_{1,1} & & & & H_{1,2\mathcal{M}} \\ & \ddots & & & \\ & & H_{n,m} & & \\ & & & \ddots & \\ H_{2\mathcal{N},1} & \cdots & & & H_{2\mathcal{N},2\mathcal{M}} \end{pmatrix} \begin{pmatrix} Q_{r,1} \\ \vdots \\ Q_{r,\mathcal{M}} \\ R_{r,1} \\ \vdots \\ R_{r,\mathcal{M}} \end{pmatrix}, \tag{5}$$

where $H_{n,m}$ represents the system gain of in-phase or in-quadrature components. Eq. (5) can be rewritten more compactly as

$$\mathbf{a}_r = \mathbf{H}\mathbf{q}_r, \quad \mathbf{H} \in \mathbb{R}^{2\mathcal{N}\times 2\mathcal{M}}, \quad \mathbf{a}_r \in \mathbb{R}^{2\mathcal{N}\times 1}, \quad \mathbf{q}_r \in \mathbb{R}^{2\mathcal{M}\times 1}, \tag{6}$$

where $\mathbf{a}_r$ is the response vector (left-hand side of Eq. (5)), and $\mathbf{q}_r$ holds the components of the rth excitation vector (column vector in the right-hand side of Eq. (5)). Combining the responses for all $r = 1,2,\ldots,2\mathcal{M}$ excitation vectors gives

$$\mathbf{A} = \mathbf{H}\mathbf{Q}, \quad \mathbf{A} \in \mathbb{R}^{2\mathcal{N}\times 2\mathcal{M}}, \quad \mathbf{Q} \in \mathbb{R}^{2\mathcal{M}\times 2\mathcal{M}}, \tag{7}$$

where $\mathbf{A}$ is the response matrix consisting of the columns $\mathbf{a}_r$, $\mathbf{H}$ is the system model, and $\mathbf{q}_r$, the corresponding excitation vectors filling the columns of $\mathbf{Q}$.

The receptance of a perfectly linear system with frequency response matrix derived from Eq. (1) can be written as

$$\boldsymbol{\alpha}(\boldsymbol{\omega}_0) \triangleq \left(-\boldsymbol{\omega}_0^2\mathbf{M} + \mathrm{i}\boldsymbol{\omega}_0\mathbf{C} + \mathbf{K}\right)^{-1}\mathbf{B}, \quad \boldsymbol{\alpha}(\boldsymbol{\omega}_0) \in \mathbb{R}^{\mathcal{N}\times\mathcal{M}}. \tag{8}$$

For such a system (see [16]), the model matrix $\mathbf{H}$ used in Eqs. (6) and (7) takes the form

$$\mathbf{H} = \left(\begin{array}{c:c} \mathrm{Re}\left(\boldsymbol{\alpha}(\omega_0)\right) & \mathrm{Im}\left(\boldsymbol{\alpha}(\omega_0)\right) \\ \hdashline -\mathrm{Im}\left(\boldsymbol{\alpha}(\omega_0)\right) & \mathrm{Re}\left(\boldsymbol{\alpha}(\omega_0)\right) \end{array}\right), \tag{9}$$

where the dashed line indicates matrix partitioning. Clearly, even the slightest nonlinearity will sometimes distort the structure of Eq. (9). Because the excitation basis, $\mathbf{Q}$, was chosen to be orthonormal, the system model can be numerically estimated without matrix inversion

$$\mathbf{H} = \mathbf{A}\mathbf{Q}^{-1} = \mathbf{A}\mathbf{Q}^{\mathrm{T}}. \tag{10}$$

Once the model has been found, Eq. (6) can now be inverted in order to find the required force-vector yielding a desired response. Normally, there are more sensors than actuators ($\mathcal{N} > \mathcal{M}$). Therefore, an over-determined least squares strategy is adopted to calculate the excitation vector – $\mathbf{q}_d$ that will result in the most suitable response vector – $\mathbf{a}_d$ with a minimum error norm [17–19]. Based upon Eqs. (6), (7) and (10), and assuming that the response matrix $\mathbf{A}$ has full rank, it is possible to calculate a unique solution for the excitation by pseudo-inversion of $\mathbf{A}$

$$\mathbf{q}_d = \mathbf{H}^{\dagger}\mathbf{a}_d = \mathbf{Q}\mathbf{A}^{\dagger}\mathbf{a}_d, \tag{11}$$

where the operator $(\cdot)^{\dagger}$ stands for pseudo-inverse, and $\mathbf{a}_d$ represents the desired spatial solution. The singular value decomposition (SVD) can be adopted to carry out the numerical computation [18].

The proposed tuning method can be used to assess the level of system nonlinearity in a particular operation regime by examining the level of agreement between the measurements-based model matrix $\mathbf{H}$ and Eq. (9).

2.2. Describing the appropriate wave response

Suppose $\mathbf{a}_d$ describes a wave travelling in a certain direction in space. This wave should have a desired wavelength λ and wavenumber $\mathcal{K}$,

$$\boldsymbol{\kappa} = 2\pi/\boldsymbol{\lambda}. \tag{12}$$

A travelling wave can be represented by

$$u(x,t) = \cos(\boldsymbol{\omega} t - \boldsymbol{\kappa} x) = \cos\boldsymbol{\omega} t \cos\boldsymbol{\kappa} x + \sin\boldsymbol{\omega} t \sin\boldsymbol{\kappa} x. \tag{13}$$

An array of sensors located at $x_1, x_2, \ldots, x_{\mathcal{N}}$, would, measure a vector of amplitudes that when decomposed into in-phase and in-quadrature components yields

$$\mathbf{a}_d = (\cos\boldsymbol{\kappa} x_1 \quad \cdots \quad \cos\boldsymbol{\kappa} x_{\mathcal{N}} \quad \sin\boldsymbol{\kappa} x_1 \quad \cdots \quad \sin\boldsymbol{\kappa} x_{\mathcal{N}})^{\mathrm{T}}, \tag{14}$$

where x_n ($n = 1,2,\ldots,\mathcal{N}$) are the measured points along the structure.

Based on Eqs. (11)–(14), it is evident that calculating the excitation forces generating a desired wave form along a structure depends on the wavelength λ. At this stage, only steady-state response at a fixed frequency is taken into consideration. Hence, the wavelength depends on the known frequency, and on the unknown properties of the medium. For example, the wavenumber of a taut string conforms to $\boldsymbol{\kappa} = \boldsymbol{\omega}/\mathrm{c}$, where ω is the vibration frequency. The wave velocity of propagation (phase velocity) c is given by $c = \sqrt{T/\boldsymbol{\rho}}$, where T is the tension and ρ is the mass density per unit length. Yet since both the tension and the material properties are unknown, the measured data can be used to discover the optimized wavelength, as discussed in Section 2.4.

2.3. Extending the method for systems exhibiting mild nonlinearity

As the system in question may not always obey strict linearity, the solution found using the proposed approach may not be optimal. An optimized solution for the case of a travelling wave is considered to be a wave of the desired amplitude for the travelling component and minimal amplitude for the standing component. A general, not necessarily linear system can be described by

$$\mathbf{a} = f(\mathbf{q},t), \tag{15}$$

where $\mathbf{a}$ is the measured response amplitude and $\mathbf{q}$ represents the excitation amplitudes. For a desired response $\mathbf{a}_d$, the excitation $\mathbf{q}_d$ should be applied. This excitation can be written as $\mathbf{q}_d = \mathbf{q}_0 + \delta\mathbf{q}$, where $\mathbf{q}_0$ is the initial guess or solution achieved using the proposed linear algorithm, and $\delta\mathbf{q}$ is a perturbation vector of small magnitude.

Since the function f and its derivatives are unknown at this stage, a set of measurements is used as a means of approximation. The approximated system model at point $\mathbf{q}_0$ is then used:

$$\mathbf{a}_d \cong \mathbf{a}_0 + \frac{\partial f(\mathbf{q}_0,t)}{\partial \mathbf{q}}\delta\mathbf{q} = \mathbf{a}_0 + \mathbf{H}(\mathbf{q}_0)\delta\mathbf{q}. \tag{16}$$

The system is excited $2\mathcal{M}$ times with excitations $\mathbf{q}_r = \mathbf{q}_0 + \delta\mathbf{q}_r$, $r = 1,2,\ldots,2\mathcal{M}$, while maintaining mutually orthogonal force perturbations $\delta\mathbf{q}_r$. Eq. (16) represents a single experiment repeated $2\mathcal{M}$ times. By collecting the force perturbations as the columns of the matrix $\Delta\mathbf{Q}$, collecting the measured response deviations from the reference point, $\delta\mathbf{a} = \mathbf{a}_r - \mathbf{a}_0$ in the matrix $\Delta\mathbf{A}$, and by using the orthonormality of $\Delta\mathbf{Q}$, one can eventually compute:

$$\mathbf{H}(\mathbf{q}_0) \cong \Delta\mathbf{A}(\Delta\mathbf{Q})^{\mathrm{T}}. \tag{17}$$

Once the model $\mathbf{H}(\mathbf{q}_0)$ has been identified at the proximity of the hyper-point $(\mathbf{a}_0, \mathbf{q}_0)$, the required perturbation to the excitation $\mathbf{q}_d = \mathbf{q}_0 + \delta\mathbf{q}_d$ can be calculated to achieve the desired solution $\mathbf{a}_d$ by rewriting Eq. (16), and using the pseudo-inverse as before:

$$\delta\mathbf{q}_{\mathrm{d}} \cong \mathbf{H}(\mathbf{q}_0)^{\dagger}(\mathbf{a}_d - \mathbf{a}_0). \tag{18}$$

A modified excitation $\mathbf{q}_d = \mathbf{q}_0 + \mu\delta\mathbf{q}_d$ can now be applied, where μ is a relaxation step size (here under-relaxation is used). The response can now be re-measured and in case the achieved response is still unsatisfactory, another set of perturbations around the corrected point is applied, and an updated model is calculated. This procedure is repeated until the error, $e = ||\mathbf{a}_d - \mathbf{H}\mathbf{q}_d||/||\mathbf{a}_d||$ becomes sufficiently small (where $||\cdot||$ stands for the Euclidean norm).

The iterative method was investigated experimentally for several sets of frequencies and excitation levels. Its significance is demonstrated below, particularly for the case of a suspected nonlinear regime in the vicinity of a structure natural frequency, where relatively large amplitudes are expected.

When the suggested algorithm is employed in the multi-frequency excitation case, the single frequency model used in Eq. (6) is replaced by a multi-frequency model in hyper-matrix form:

$$\left(\begin{array}{c} \mathbf{a}^{1} \\ \hdashline \vdots \\ \hdashline \mathbf{a}^{\mathcal{P}} \end{array}\right) = \left(\begin{array}{c:c:c} \mathbf{H}^{1,1} & \cdots & \mathbf{H}^{1,\mathcal{P}} \\ \hdashline \vdots & \vdots & \vdots \\ \hdashline \mathbf{H}^{\mathcal{P},1} & \cdots & \mathbf{H}^{\mathcal{P},\mathcal{P}} \end{array}\right) \left(\begin{array}{c} \mathbf{q}^{1} \\ \hdashline \vdots \\ \hdashline \mathbf{q}^{\mathcal{P}} \end{array}\right). \tag{19}$$

The hyper-matrix model combines the contributions of several harmonics $h\omega_0$, $h = 1,2,\ldots,\mathcal{P}$. As above, the dashed lines signify matrix and vector partitioning. The remaining identification procedure is the same as for a single frequency, with the dimensions adjusted accordingly. The notation $\mathbf{H}^{k,l}$ signifies the model of the response at the kth harmonic to excitation at the lth harmonic. It should be noted that for a perfectly linear system, the off-diagonal blocks in Eq. (19) are all zeros, meaning that excitation at a certain frequency results in a response at that same frequency only.

2.4. Wavelength optimization

Although the tuning process may seem straightforward, there is not always a physically meaningful solution. One example is the attempt to generate a travelling wave whose wavelength does not comply with the excitation frequency. Another is the attempt to tune a response at one of the structure's natural frequencies, where most structures amplify a standing wave due to one dominant eigenmode (mode of vibration).

In order to tune a structure's response at a given frequency with a physically meaningful vibration pattern, the appropriate wavelength must be determined. One option is to start with a reasonable initial wavelength λ_0, and to calculate the desired response $\mathbf{a}_d(\lambda_0)$using Eqs. (12) and (14). The excitation forces are determined using Eq. (11)

$$\mathbf{q}_d(\boldsymbol{\lambda}_0) = \mathbf{H}^{\dagger}\mathbf{a}_d(\boldsymbol{\lambda}_0) = \mathbf{Q}\mathbf{A}^{\dagger}\mathbf{a}_d(\boldsymbol{\lambda}_0). \tag{20}$$

Now a model-dependent error is defined as

$$\mathbf{e}(\boldsymbol{\lambda}_0) = \mathbf{a}_d(\boldsymbol{\lambda}_0) - \mathbf{H}\mathbf{q}_d(\boldsymbol{\lambda}_0), \tag{21}$$

and a normalized mismatch function is defined as

$$J_{\mathrm{mis}}(\boldsymbol{\lambda}_0) = \frac{\|\mathbf{e}(\boldsymbol{\lambda}_0)\|}{\|\mathbf{a}_d(\boldsymbol{\lambda}_0)\|}. \tag{22}$$

It is important to note that this process would not require any additional experiments, once the model was obtained. The minimum of $J_{\mathrm{mis}}(\lambda)$ yields the most suitable wavelength at the specific excitation frequency, which also hints at the medium's properties (such as the dispersion equation). An optimal wavelength λ_{opt} minimizes the mismatch function $J_{\mathrm{mis}}(\lambda)$. When tuning a flexural travelling wave, choosing a non-optimal wavenumber yields a response composed of both travelling and undesired standing waves.

The same wavelength optimization procedure can also be employed to find the optimal wavelength along a two-dimensional structure of Cartesian coordinates, such as a membrane. For example, if a travelling wave is to be tuned to travel at a desired direction – say θ degrees from the positive x-axis – then the desired response of unit amplitude is

$$u(\mathbf{r},t) = \cos(\boldsymbol{\omega}t - \boldsymbol{\kappa}\cdot\mathbf{r}) = \cos\boldsymbol{\omega}t\cos(\boldsymbol{\kappa}\cdot\mathbf{r}) + \sin\boldsymbol{\omega}t\sin(\boldsymbol{\kappa}\cdot\mathbf{r}), \tag{23}$$

where $\boldsymbol{\kappa}$ is the wave vector and $\mathbf{r}$=(x,y) is a position vector. Hence, the desired discrete spatial response to be substituted into Eq. (11) is

$$\mathbf{a}_d = (\,\cos(\boldsymbol{\kappa}\cdot\mathbf{r}_1) \quad \cdots \quad \cos(\boldsymbol{\kappa}\cdot\mathbf{r}_{\mathcal{N}}) \quad \sin(\boldsymbol{\kappa}\cdot\mathbf{r}_1) \quad \cdots \quad \sin(\boldsymbol{\kappa}\cdot\mathbf{r}_{\mathcal{N}})\,)^{\mathrm{T}}, \tag{24}$$

where $\mathbf{r}_n$, is the position of the nth point along the membrane ($n = 1,2,\ldots,\mathcal{N}$). The wavelength λ is then

$$\boldsymbol{\lambda} = \frac{2\pi}{\|\boldsymbol{\kappa}\|}, \quad \boldsymbol{\kappa} = (\,\boldsymbol{\kappa}_x \quad \boldsymbol{\kappa}_y\,), \quad \boldsymbol{\kappa}_x = \|\boldsymbol{\kappa}\|\cos\boldsymbol{\theta}, \quad \boldsymbol{\kappa}_y = \|\boldsymbol{\kappa}\|\sin\boldsymbol{\theta}. \tag{25}$$

The optimal wavelength can be estimated by substituting Eqs. (24) and (25) into Eqs. (20)–(22).

Borrowing two terms from systems control theory, the wavelength optimization stage can be viewed as a method to assess and affect the level of controllability and observability of a specific configuration. The expression in Eq. (22) tells us how close we can approximate the desired response vector $\mathbf{a}_d(\lambda_0)$ by using any combination of the existing array of actuators $\mathbf{q}_d(\lambda_0)$, while using the present configuration represented by the model $\mathbf{H}$.

2.5. Wave identification methods in brief

Two main methods are used here to identify whether the flexural waves are standing or travelling, and in what direction. The first method makes use of an ellipse fitted to the complex amplitude of an one-dimensional structure's response, and the second uses power-flow for one- and two-dimensional systems.

2.5.1. Fitting an ellipse to a complex response

A measured one-dimensional system can be analyzed in two ways. The first approach uses a plot of the measured vibration complex amplitude with phase relative to a common reference, as described in [20]. Plotting the real vs. imaginary component of the measured amplitude along the structure yields a perfect circle for a pure travelling wave, a straight line for a pure standing wave, and a skewed ellipse for any other combination (see for example Fig. 8).

2.5.2. Power-flow

The second approach is the power-flow approach, used to analyze vibration patterns in 1D and 2D systems [21–24]. The vector of temporal mean power-flow per cycle of a 2D system, $\langle \mathbf{P}(x,y) \rangle$, is defined by

$$\langle \mathbf{P}(x,y) \rangle = (\langle P_x(x,y) \rangle \quad \langle P_y(x,y) \rangle). \tag{26}$$

As an example, the mean power-flow components P_x,P_y of a membrane of unit tension force are computed by

$$\begin{aligned} \langle P_x \rangle &= -\frac{1}{2}\frac{\partial u(x,y,t)}{\partial t}\left(\frac{\partial u(x,y,t)}{\partial x}\right)^* \\ \langle P_y \rangle &= -\frac{1}{2}\frac{\partial u(x,y,t)}{\partial t}\left(\frac{\partial u(x,y,t)}{\partial y}\right)^*, \end{aligned} \tag{27}$$

where $u(x,y,t)$ is the complex amplitude, and the operator $(\cdot)^*$ represents a complex conjugate. The power-flow expression in Eq. (27) is complex. The real part $\mathrm{Re}(\langle P \rangle)$ is the active power-flow of the wave, signifying the actual power carried away with the wave. The imaginary part $\mathrm{Im}(\langle P \rangle)$is the reactive power. This power remains in the structure, fluctuating back and forth between nodal points or nodal lines. The closer the vibration is to a pure travelling wave, the more actively does the power-flow with the wave. On the other hand, the mean active power-flow per period is zero when the wave is standing. In general, different amounts of power-flow in every direction. The power-flow vector field $\langle \mathbf{P}(x,y) \rangle$ is indicated by the arrows (in Fig. 3) showing the magnitude and direction of the mean real part of the vibration's power-flow per cycle. When the vibration pattern consists of a mixture of standing and travelling waves, the average power-flow per cycle has no specific direction or magnitude (Fig. 3(a)). In contrast, when the vibration consists of pure travelling waves, the power-flow has a uniform magnitude and direction (Fig. 3(b)).

3. Results

This section provides numerical and experimental results of the proposed tuning method. The numerical analysis is based on FE model written in Matlab™. For the 1D string case, linear elements are used, and in the case of a 2D membrane, bi-linear elements are employed. The experiments are conducted on electro-mechanical devices incorporating either a string or a membrane as the vibrating structure.

3.1. Experimental layout overview

The experimental system (Fig. 4) comprises a PC, a dSPACE real-time control and I/O, a Polytech scanning laser doppler vibrometer (LDV), and the device being tested. The inspected vibrating system consists of either a stainless steel string

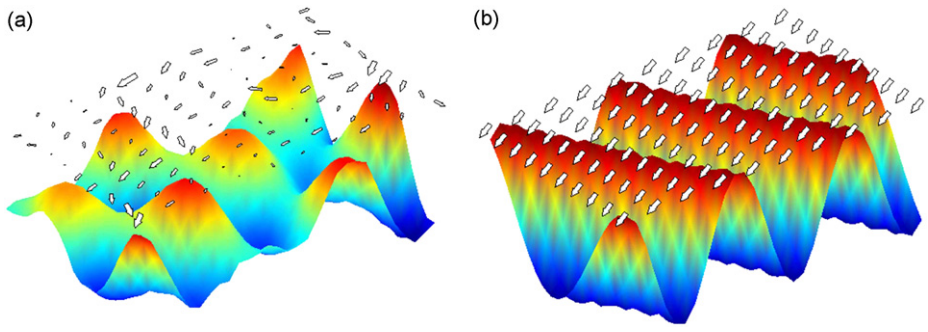

Fig. 3. Power-flow of simulated membrane model: (a) mixed travelling and standing waves and (b) tuned travelling waves in desired direction.

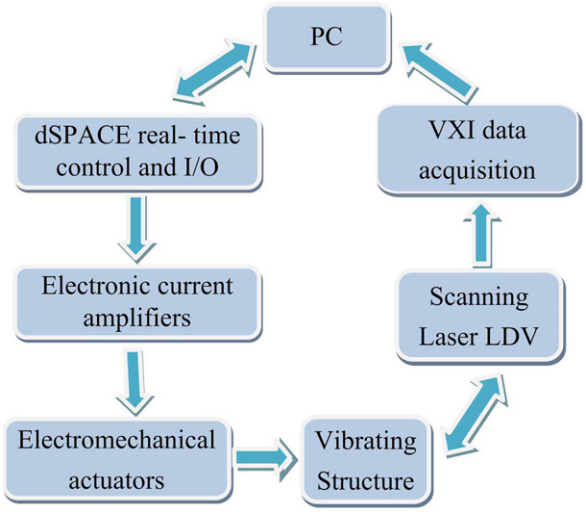

Fig. 4. Experiment system layout.

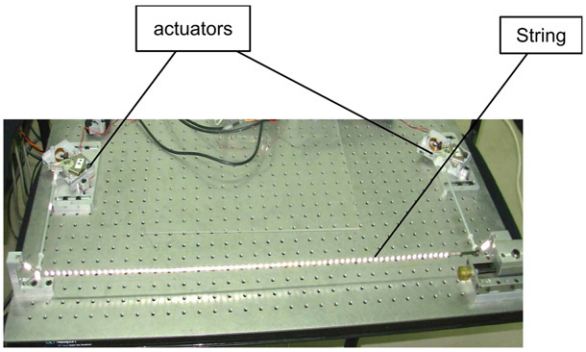

Fig. 5. Experimental system consisting of a taut string and two exciters scanned by LDV.

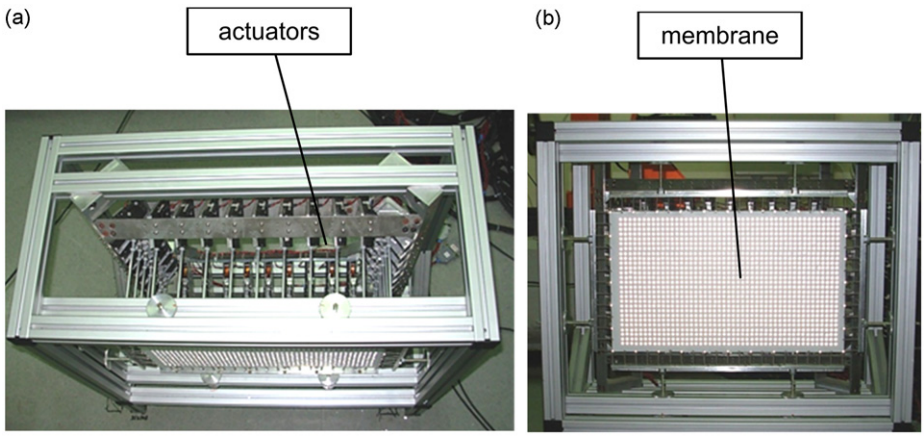

Fig. 6. Membrane experimental system: (a) top view and (b) front view.

(Fig. 5) excited by two actuators, or a polyurethane membrane excited by 32 actuators (Fig. 6). The membrane is taut and connected to the frame by circumferential springs. A Matlab^{TM} program running on the PC commands the real-time dSPACE environment and a VXI data acquisition system (VXITech, VT1433B). The dSPACE system controls an external power amplifier containing current drivers. The amplitude and phase of the 32 voice-coil actuators are controlled by 32

digital-to-analogue converters. The vibrating string and membrane structures are equipped with 73 and 1263 diffusivity enhancing stickers, respectively, that are measured by the LDV. The LDV output is filtered (LP Filter of 2.56 kHz), sampled (at 6.55 kHz), and recorded by the VXI sampling unit connected to the PC via firewire. The frequencies of interest are in order of 10^1–10^2 Hz. The recorded digital data is sine-fitted according to the input frequencies and their harmonics, then it is further processed using a dedicated Matlab^{TM} code implementing the described tuning method.

3.2. Numerical and experimental tuning results for one-dimensional string system

In this section, numerical and experimental results are presented for a taut string model and experimental device. These results are used to validate the proposed tuning method for single and multi-frequency tuning, including wavelength optimization and model matrix analysis of 1D structures.

3.2.1. Single frequency tuning

The wavelength optimization described in Section 2.4 (Eqs. (20)–(22)) was verified by simulations on the FE string model, with artificial noise added to the simulated measurements. The results can be seen in Fig. 7(a).

A definite global minimum is observed for the quality measure (mismatch function). Nevertheless, as might be expected some local minima are also present in the rational fractions of λ_0 (that might affect some minimum-seeking solvers). Similar behavior was found during the optimization routine applied to experimentally measured data from the string device, as can be seen in Fig. 7(b).

After model identification and wavelength optimization were completed experimentally, the two actuators were tuned to generate several vibration patterns of standing wave and travelling wave at some distance from the string boundaries. A third combination representing an arbitrary mixture of standing and travelling waves was also measured for comparison. The measured complex response of the three cases was plotted on the complex plane, and the corresponding real and imaginary components of the mean power-flow are given in Fig. 8. As expected, the complex response of a standing wave traces a straight line and the mean active power-flow approaches zero (Fig. 8(a) and (d)). In contrast, the complex response of a travelling wave (Fig. 8(c) and (f)) approaches a circle, and the mean active power-flow approaches a nonzero uniform value, whose sign represents the direction of wave propagation. The imaginary component of the mean power-flow represents the reactive power, i.e. the power cycling within the string system. Note that for the standing and mixed-waves cases, the imaginary component oscillates along the string, while for the pure travelling wave this part approaches zero (Figs. 8(d)–(f), respectively).

3.2.2. Multi-frequency tuning

For the sake of improved interpretation of the measured results of a multi-frequency response, the dynamic compliance of the string was measured in the relevant frequency domain, and is given in Fig. 9. The curve shape corresponds with the obtained results, as discussed below.

Two multi-frequency tuning sets of measurements are presented here. Each set includes the simultaneous tuning of three harmonics. The string was first tuned at 33, 66, 99 Hz. At these frequencies, the structure's response amplitude gain is rather moderate (see Fig. 9), a finding addressed in analyzing the topology of the model matrix **H**. The string was tuned to incorporate three travelling waves simultaneously at the three harmonics 33, 66, 99 Hz of the same 0.1 mm amplitude. Fig. 10 shows the measured complex response after one and five perturbations. The final result yields three circles of approximately the same radius, indicating a response comprising three travelling waves with the same amplitude of about 0.1 mm.

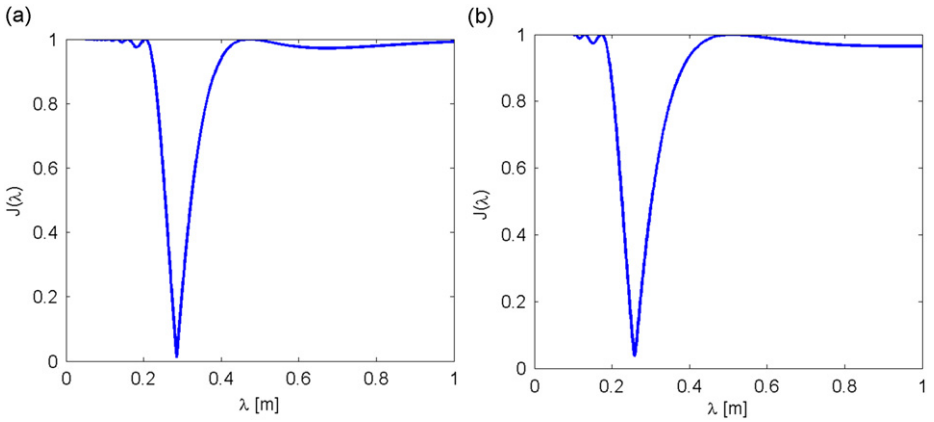

Fig. 7. String: response mismatch vs. wavelength (Eq. (22)): (a) by simulation and (b) by measured data.

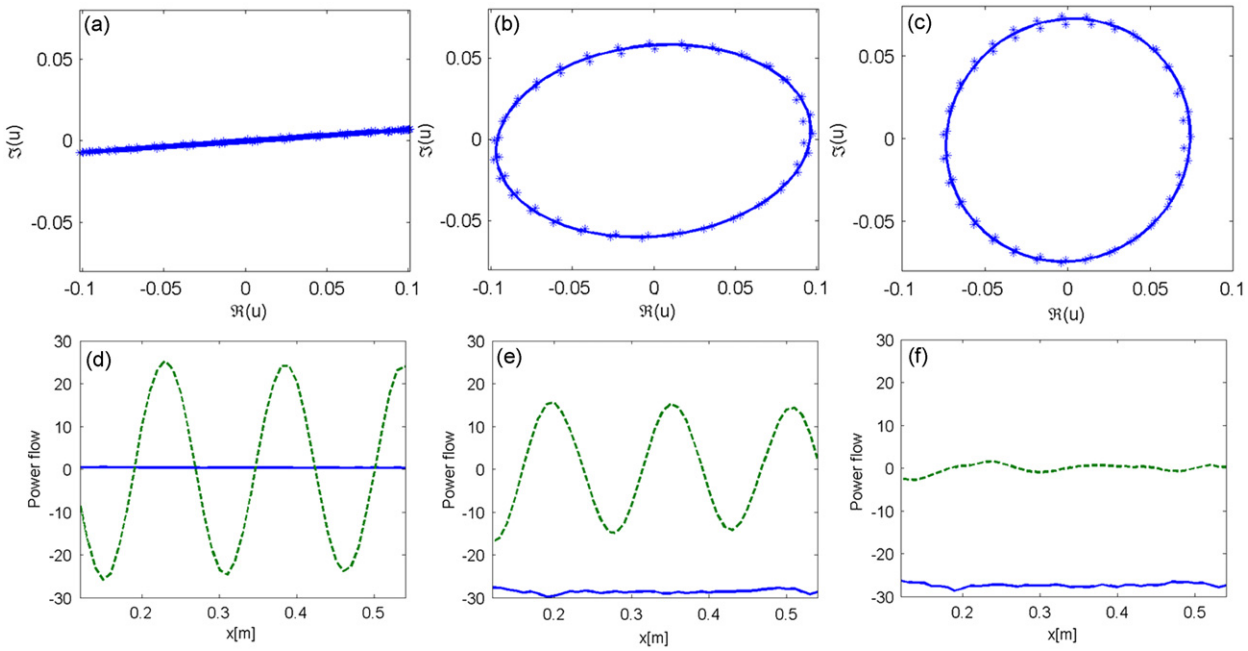

Fig. 8. (a) Complex measured response in (mm) of tuned standing wave: (b) mixed waves and (c) tuned travelling wave. ∗ Measured, — fitted; (d) real and imaginary power-flow in arbitrary units of standing waves, (e) mixed waves and (f) standing waves, — real power-flow, - - imaginary power-flow.

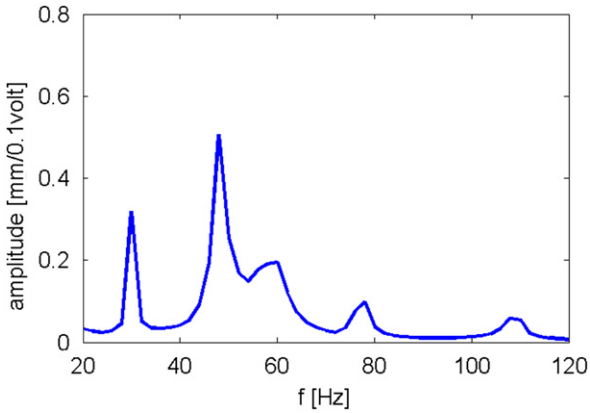

Fig. 9. Measured typical dynamic compliance of the string.

Yet when the string's structure was measured and analyzed at the second frequency set 30, 60, 90 Hz, which is closer to natural frequencies (see Fig. 9), a different model was identified. The string device was tuned for a travelling wave at 60 Hz only. Undesired responses at 30 and 90 Hz were actively decayed. These parasitic harmonics were expected to arise due to cross-coupling in the response, as discussed in Section 3.2.4. The results after one and twelve perturbations are shown in Fig. 11. The initial response in Fig. 11(a) shows a very thin ellipse in the first harmonic, indicating an undesired significant standing wave at 30 Hz with an amplitude of about 1 mm. The final response shows a circle with a radius of approximately 0.1 at 60 Hz with remaining small responses of about 0.02 at 30 and 90 Hz. This indicates a nearly pure travelling wave was created at 60 Hz at the desired amplitude of 0.1 mm with residual responses of about 0.02 mm at 30 and 90 Hz. These results indicate that nonlinear adaptation via perturbation facilitates reduction of an unwanted dominant standing wave by two orders of magnitude.

Tuning at the frequency set 30, 60, 90 Hz required more perturbation steps than at 33, 66, 99 Hz to sufficiently approach the desired response. Clearly, the high amplitudes gave rise to some nonlinear coupling between the various harmonics.

3.2.3. Real-time wave measurement—verification

The real-time velocities of two points along a string undergoing a single frequency excitation were measured simultaneously using two LDVs. The LDVs first measured the same point and then measured two points displaced a quarter

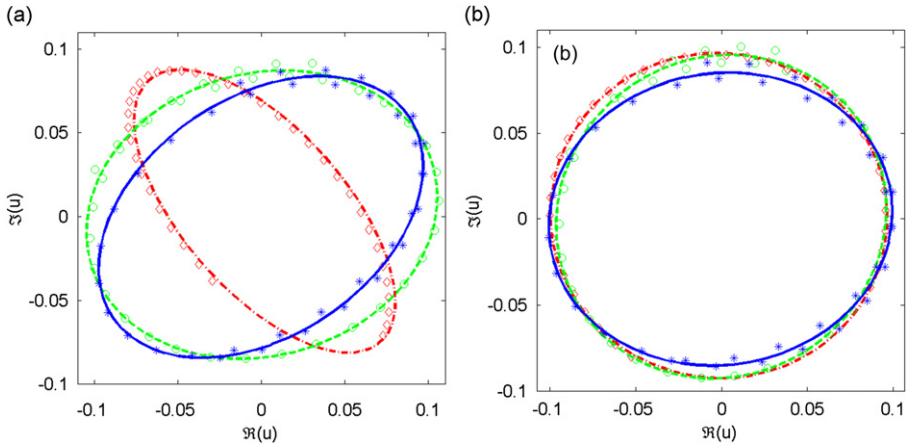

Fig. 10. Measured complex response of tuned travelling waves at 33, 66, 99 Hz simultaneously: (a) after one iteration, and (b) after five iterations. (◇) Measured at 33 Hz, (○) measured at 66 Hz, (∗) measured at 99 Hz, (— · —) fitted at 33 Hz, (– –) fitted at 66 Hz and (—) fitted at 99 Hz.

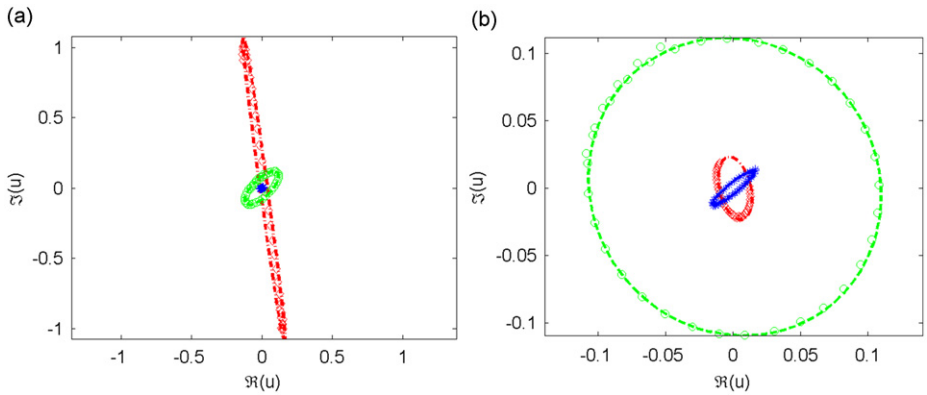

Fig. 11. Measured complex response of tuned travelling waves at 60 Hz while simultaneously decaying parasitic responses at 30 and 90 Hz: (a) after one iteration, (b) after 12 iterations. (◇) Measured at 30 Hz, (○) measured at 60 Hz, (∗) measured at 90 Hz, (— · —) fitted at 30 Hz, (– –) fitted at 60 Hz, and (—) fitted at 90 Hz.

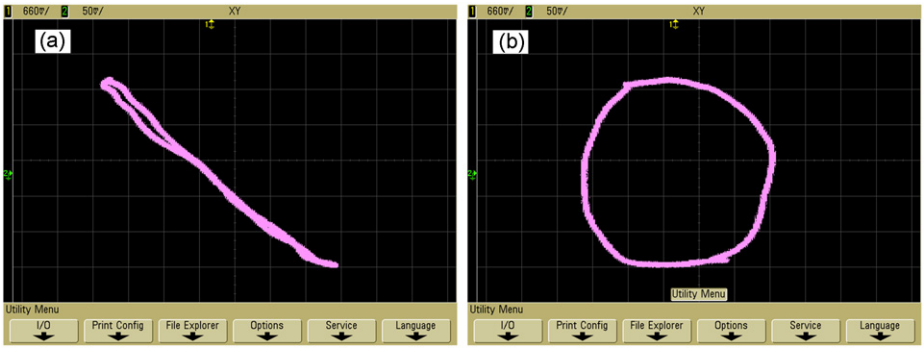

Fig. 12. Lissajou diagram of two time-response signals measured at points along a string experiencing travelling wave: (a) at the same location and (b) quarter wavelength apart.

of a wavelength apart. The two measured signals were connected to the x and y channels of an oscilloscope. Measuring the same point should yield a straight line in the Lissajou diagram, while measuring two points separated by a quarter wavelength while assuming travelling waves with only one dominant harmony (linear system) should yield a perfect circle. The two measurements at 100 Hz are depicted in Fig. 12(a) and (b), respectively. Real-time Lissajou plots provide an accurate verification of the fact that a monochromatic travelling wave has been formed. The alternative approach that uses

the complex amplitude data measured along the structure uses an inevitable curve-fit stage where the average results can only be displayed.

3.2.4. Model matrix **H** analysis—measured data

The single-frequency model matrix components defined in Eq. (5) were first examined for single frequency tuning under moderate input amplitudes at 85 Hz, far from any of the structure's natural frequencies (see Fig. 9). The result is depicted in Fig. 13, where the *x*- and *y*-axis stand for the **H** matrix row and column indices, and the numerical value of each element is color coded. The four columns represent the cosine and sine terms of the two actuators, ($2\mathcal{M}=4$), and the rows represent the cosine and sine terms of the 38 measured points ($2\mathcal{N}=76$) along the string. The upper left and lower right blocks in Fig. 13, separated by dashed lines, signify the structure's cosine terms response to the cosine terms of the input, and the same applies for the sine terms, respectively (see Eqs. (3)–(5) and (8), (9)). The off-diagonal blocks are the structure's response in cosine terms to sine input terms, and vice versa.

The anticipated block structure as given in Eq. (9) is clearly observed, implying a certain level of linearity in that particular operation regime. The off-diagonal terms are clearly smaller in magnitude than the diagonal blocks, indicating a negligible phase lag implying low damping and an excitation frequency far enough from any natural frequency. The diagonal blocks are nearly identical, and the off-diagonal terms have opposite signs, as predicted by Eq. (9).

In accordance with Eq. (19), the multi-frequency matrix model was analyzed for the two sets of frequencies: 30, 60, 90 and 33, 66, 99 Hz. The results are presented in Fig. 14. The components in Fig. 14 are divided into bigger and smaller blocks by wide and thin dashed lines, respectively. The wider dashed lines indicate the frequency blocks, and the thinner indicate cosine and sine terms as before. The larger diagonal blocks represent the response at a given frequency to excitation at the same frequency, while the larger off-diagonal blocks represent the excitation of super- or sub-harmonics, i.e. frequency cross-coupling. The anticipated linear model can be seen in Fig. 14(a) for 33, 66, 99 Hz, where the large off-diagonal blocks approach zero, indicating negligible cross-coupling. In Fig. 14(b), however, the string structure model for the frequency set 30, 60, 90 Hz, i.e. closer to the natural frequencies, is different. The model differs both in its diagonal blocks and in its off-diagonal blocks. A strong asymmetric sub-harmonic response is observed at $\mathbf{H}^{1,2}$ (notation according to Eq. (19)), indicating a response at 30 Hz to excitation at 60 Hz. The upper left block of Fig. 14(b) represents $\mathbf{H}^{1,1}$, or the response at 30 Hz to excitation at 30 Hz. An examination of the smaller blocks of $\mathbf{H}^{1,1}$ reveals more dominant off-diagonal components, indicating in-quadrature response, as expected for a structure excited close to one of its natural frequencies. The results shown here suggest that unsuccessful choice of excitation frequency can distort the obtained response considerably. Still, when the nature of these distortions, i.e. nonlinear behavior causing harmonics, is accounted for, their effect can be identified and nullified.

3.3. Numerical and experimental tuning results of two-dimensional membrane system

This section presents the numerical and experimental results of tests carried out on a membrane using the proposed method. A closed form analytical solution is compared with the tuning method results for an ideal case to validate the

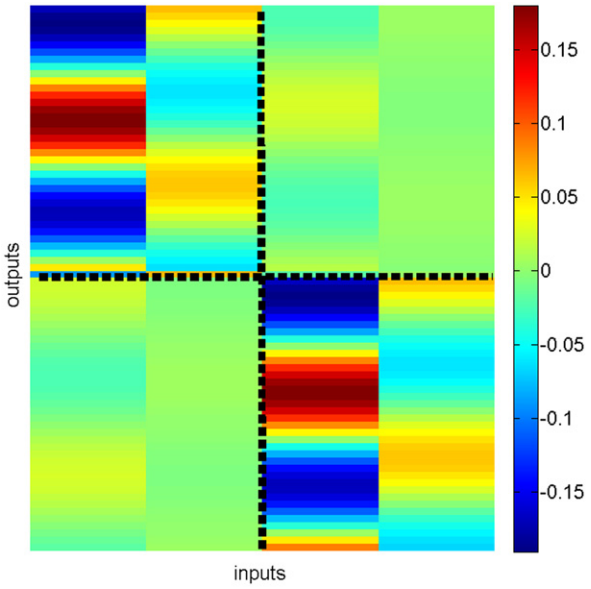

Fig. 13. Model matrix (**H**) components—measured string model at 85 Hz (Eq. (10)).

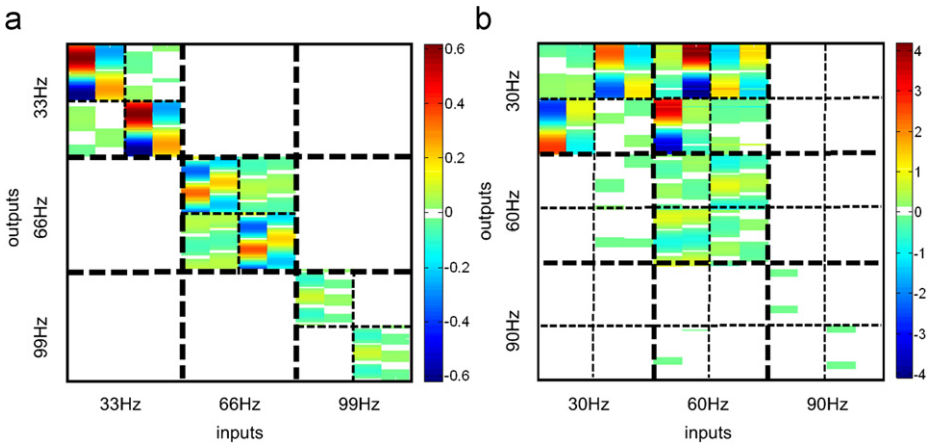

Fig. 14. Measured string multi-frequency model matrix components: (a) at 33, 66, 99 Hz and (b) at 30, 60, 90 Hz (Eq. (19)).

tuning method for two-dimensional systems. The wavelength optimization procedure, the model matrix analysis, and the ability to create non-trivial response patterns are all examined.

3.3.1. *Numerical comparison with analytic solution of travelling waves in a rectangular membrane*

According to [12,21], the optimal spatial force distribution for generating travelling waves on a membrane is along the edges. The problem of determining the temporal force distribution along the edges of a free rectangular membrane yielding a travelling wave of desired wavelength and direction has a closed form solution [12]. A complex, two-dimensional, travelling wave of unit amplitude, frequency ω, and wave vector $\boldsymbol{\kappa} = (\kappa_x \quad \kappa_y)$ can be written as

$$u(x,y,t) = e^{-\mathrm{i}(\kappa_x x + \kappa_y y - \omega t)} \tag{28}$$

in Cartesian coordinates (x,y), where $\mathrm{i} \equiv \sqrt{-1}$.

According to [21], the analytical expressions for the continuous complex forces along the four edges of the rectangular membrane, $(f_1 f_2 f_3 f_4)$ to generate this wave are

$$\begin{aligned} f_1(y) &= \mathrm{i}T\kappa_x e^{-\mathrm{i}\kappa_y y}, \quad f_2(y) = -\mathrm{i}T\kappa_x e^{-\mathrm{i}(\kappa_x L_x + \kappa_y y)}, \\ f_3(x) &= \mathrm{i}T\kappa_y e^{-\mathrm{i}\kappa_x x}, \quad f_4(x) = -\mathrm{i}T\kappa_y e^{-\mathrm{i}(\kappa_y L_y + \kappa_x x)}, \end{aligned} \tag{29}$$

where T is the tension and L_x, L_y are the membrane's dimensions. In the application of discrete forces on the FE model nodes, the continuous analytical force expressions are spatially discretized, as shown below. When a single element is described using local Cartesian coordinates (ξ,η), the four shape functions vector $\boldsymbol{\Phi}(\xi,\eta)$ per element is

$$\boldsymbol{\Phi} = \left(\frac{1}{4}(1-\xi)(1-\eta) \quad \frac{1}{4}(1+\xi)(1-\eta) \quad \frac{1}{4}(1+\xi)(1+\eta) \quad \frac{1}{4}(1-\xi)(1+\eta) \right). \tag{30}$$

Now, the forces acting on each of the element's nodes, $\mathbf{Q}_e$, are calculated by projecting the spatial continuous force $f(\xi,\eta)$ on the shape functions

$$\mathbf{Q}_e = \frac{ab}{4} \int_{-1}^{1} \int_{-1}^{1} \boldsymbol{\Phi}(\xi,\eta)^{\mathrm{T}} f(\xi,\eta) \, \mathrm{d}\xi \, \mathrm{d}\eta, \tag{31}$$

where a and b are the element's dimensions. The analytically calculated discretized complex forces and the tuned forces are plotted on the complex plane in Fig. 15(a). For the sake of actual physical insight, the real components of the forces are plotted in Fig. 15(b) along the membrane edges in their correct location of operation. Good agreement between the analytical and tuned forces can be observed.

It should be noted, however, that the analytical solution requires complete knowledge about all of the system parameters (tension, mass density, exact boundary conditions, etc.), and is sensitive to any changes. Moreover, for complicated boundary conditions such as elastic support or inhomogeneous structure, the analytical solution becomes tedious and sometimes unobtainable. The proposed tuning method overcomes these difficulties inherently.

3.3.2. *Wavelength optimization*

Tuning travelling waves along a membrane at a given frequency necessitates a suitable wavelength. As explained in Section 2.4 (Eqs. (20)–(22)), the mismatch function can be used to determine the optimal wavelength. The simulation and experimental results of wavelength optimization in the membrane are depicted in Fig. 16.

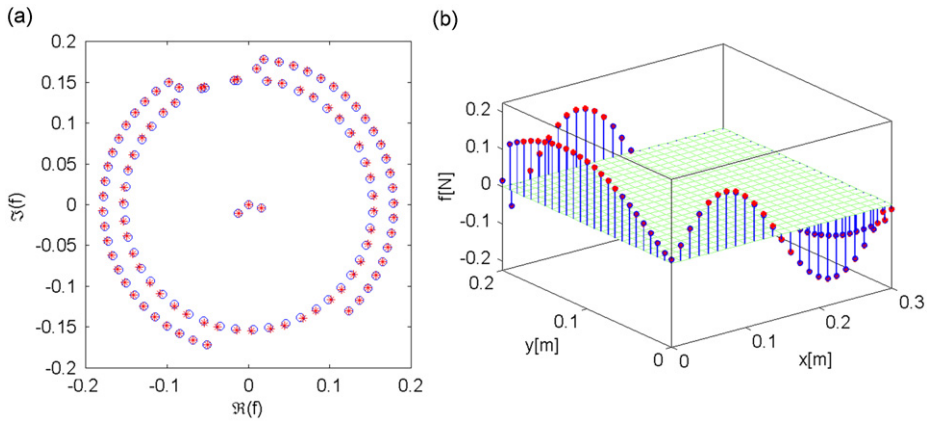

Fig. 15. Comparison between analytic and tuned forces: (a) complex and (b) real components. (○) and (♀) tuned, (*) analytic.

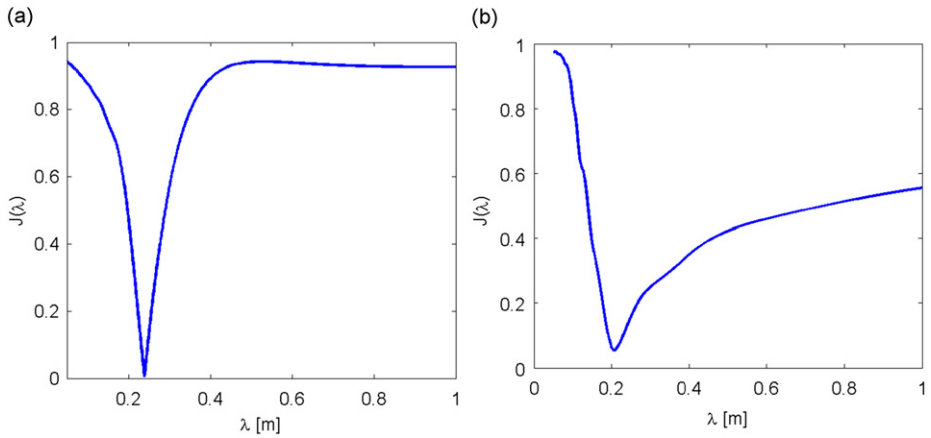

Fig. 16. Membrane response mismatch vs. wavelength (Eq. (22)): (a) by simulation and (b) by measured data at 40 Hz.

The wavelength optimization method does not require any information about the model's geometry or the material constants. Based on pure experimentally obtained data, the offline optimization searches for the best wavelength favored by the system under test conditions. As in the one-dimensional system (Fig. 7), a clear global minimum can be seen in Fig. 16.

3.3.3. *Model matrix **H** analysis—measured data*

Eq. (10) was used to calculate a membrane's single frequency model based on measured data incorporating the excitation of 32 actuators ($2\mathcal{M}=64$) and 589 measured points ($2\mathcal{N}=1178$) at an excitation frequency of 40 Hz. According to the measured dynamic compliance of the membrane (given in Fig. 17) the membrane gain is moderate at the chosen excitation frequency, so that linear behavior can be expected.

The linearity level was examined by inspecting the measured model block-matrix structure depicted in Fig. 18, as in the string case (Fig. 13).

Clearly, the hyper block-matrix shown in Fig. 18 has the same topology as that of Eq. (9) and is thus an indication of high linearity at the chosen operation regime.

3.3.4. *Tuning single and multi-frequency travelling waves and vortexes*

The tuning algorithm was tested numerically to generate a travelling wave with a given amplitude and wave vector $\boldsymbol{\kappa}$, as given in Eqs. (24) and (25). The membrane was modeled by FE scheme with uniform tension and concentrated masses and springs at each actuation node, in this case only along the boundaries. Simulated results along with the real mean power-flow are shown in Fig. 2(b). The membrane experiment device (see Fig. 6) was used for the two-dimensional tuning experiments. The surface of the membrane, at some distance from the boundaries, was tuned for travelling waves at

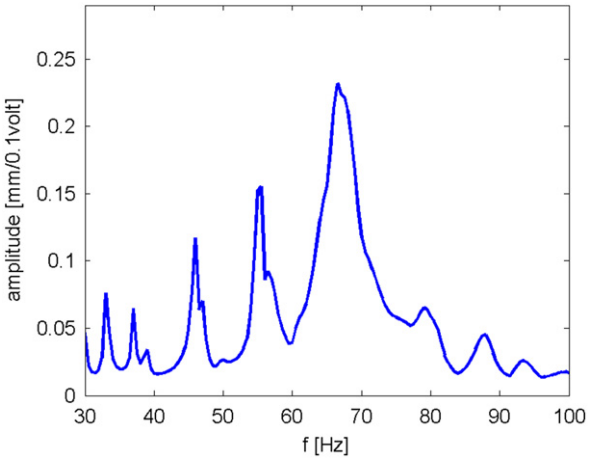

Fig. 17. Measured typical dynamic compliance of the membrane.

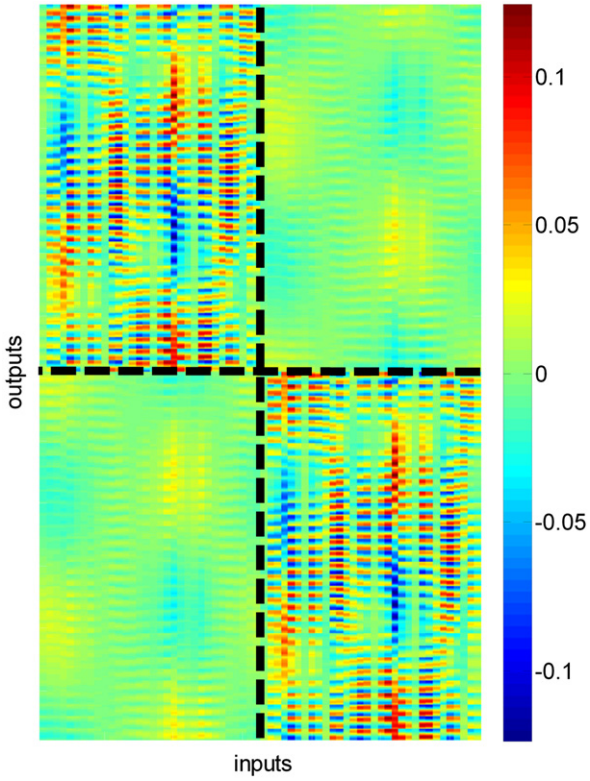

Fig. 18. Model matrix (**H**) components—measured membrane model at 40 Hz (Eq. (10)).

different directions by a number of actuators (here 6–10) located along the boundaries. The measured results depicted in Fig. 19 show that a desired wave can be tuned by actuators residing far from the tuned area.

The location of the actuators can be visibly traced by noting the area with larger amplitudes, as depicted in Fig. 19(c) and (d). According to the calculated power-flow given by the arrows in Fig. 19, the tuned area shows the desired travelling wave response, while the peripheral area exhibits a periodic arbitrary vibration.

The tuning algorithm was next used numerically to simulate a 2D response incorporating several harmonics in the form of a truncated Fourier series shaped as a travelling triangular wave. The tuning algorithm should tune each harmonic to yield a travelling wave at a specific amplitude, and all the waves having different frequencies should travel in-phase and at the same direction of propagation. The truncated Fourier series, consisting of $\mathcal{P}$ harmonics, describing such a response

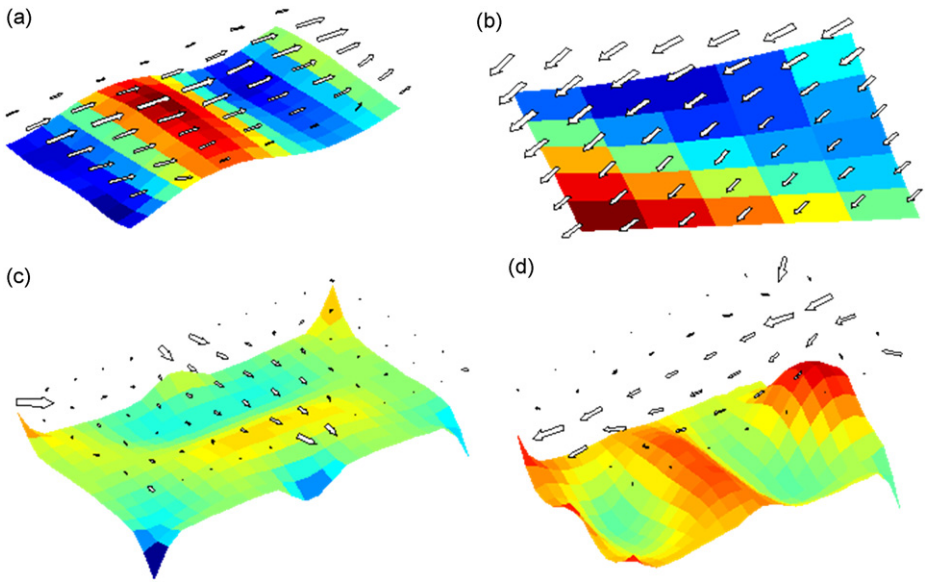

Fig. 19. Measured travelling wave along a membrane with the real mean power-flow at four different directions of advance: (a) mid membrane tuned and measured, θ=0°, (b) mid membrane tuned and measured, θ=45°, (c) mid membrane tuned all membrane measured, θ=90°, (d) mid-membrane tuned all membrane measured, θ=180° (excitation using 6–10 actuators at 40 Hz).

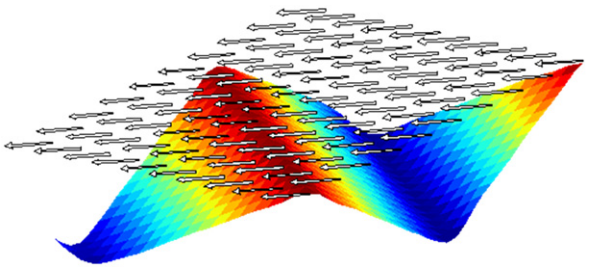

Fig. 20. Power-flow of triangular travelling wave of 5 harmonics (from 10 Hz)—FE model simulation.

can be written as

$$u(x,y,t)=\frac{8}{\pi^2}\sum_{n=1}^{\mathcal{P}}\frac{1}{(2n-1)^2}\cos(\boldsymbol{\kappa}_n\cdot\mathbf{r}-(2n-1)\boldsymbol{\omega}_0 t)$$

$$=\frac{8}{\pi^2}\sum_{n=1}^{\mathcal{P}}\frac{1}{(2n-1)^2}(\cos(\boldsymbol{\kappa}_n\cdot\mathbf{r})\cos((2n-1)\boldsymbol{\omega}_0 t)+\sin(\boldsymbol{\kappa}_n\cdot\mathbf{r})\sin((2n-1)\omega_0 t)), \tag{32}$$

where ω_0 is the basic harmonic, $\boldsymbol{\kappa}_n$ is the nth wave vector, and $\mathbf{r}$ is the position vector as defined below Eq. (23). The simulated response with the power-flow analysis of a series of five harmonics is given in Fig. 20.

Other series such as a rectangular travelling wave or a half-sine pulse can be similarly approximated. Indeed, they were also simulated successfully, though are not described here due to space limitations.

The proposed method was next used to tune rotating waves in a rectangular membrane at a variety of circular wavelengths and frequencies. To this end, the desired response was presented as a separable time–space function in terms of sine/cosine coefficients. The function can be written in polar coordinates as

$$u(r,\theta,t)=\sin(\kappa_r r)\cos(\kappa_\theta\theta-\omega t), \tag{33}$$

where κ_r and κ_θ are scalars dictating the spatial frequencies (wavenumbers) along the radius and along the circumference, respectively. To satisfy circular continuity, κ_θ must be an integer. The temporal frequency of the excitation governing the rotation speed is ω. Transforming Eq. (33) into Cartesian coordinates and expanding yields

$$u(x,y,t)=\sin\left(\boldsymbol{\kappa}_r\sqrt{x^2+y^2}\right)\cos(\boldsymbol{\kappa}_\theta\arctan(y/x)-\boldsymbol{\omega}t)$$

$$=\sin\left(\boldsymbol{\kappa}_r\sqrt{x^2+y^2}\right)(\cos(\boldsymbol{\kappa}_\theta\arctan(y/x))\cos\boldsymbol{\omega}t+\sin(\boldsymbol{\kappa}_\theta\arctan(y/x))\sin\boldsymbol{\omega}t). \tag{34}$$

As before, κ_r (and κ_θ) are also determined by minimizing the two dimensional mismatch function $J_{\mathrm{mis}}(\kappa_r,\kappa_\theta)$ in order to establish the optimal wavelength given a predetermined frequency, where

$$J_{\mathrm{mis}}(\boldsymbol{\kappa_r},\boldsymbol{\kappa_\theta}) = \frac{\|\mathbf{e}(\boldsymbol{\kappa_r},\boldsymbol{\kappa_\theta})\|}{\|\mathbf{a}_d(\boldsymbol{\kappa_r},\boldsymbol{\kappa_\theta})\|}, \tag{35}$$

$\mathbf{a}_{\mathrm{d}}(\boldsymbol{\kappa_r},\boldsymbol{\kappa_\theta})$ is the desired response, and $\mathbf{e}(\boldsymbol{\kappa_r},\boldsymbol{\kappa_\theta})$ is the difference between the desired response and the predicted model-based response. In this case, the function, $J_{\mathrm{mis}}(\kappa_r,\kappa_\theta)$, must be minimized similar to in Eqs. (21) and (22), where here the optimization controls two parameters. Fig. 21 shows a typical optimization surface of $J_{\mathrm{mis}}(\kappa_r,\kappa_\theta)$ for a membrane FE model together with experimentally measured data ($\kappa_r \neq 0$). Satisfactory responses are achievable when choosing the pair (κ_r,κ_θ) at any of the minima of $J_{\mathrm{mis}}(\kappa_r,\kappa_\theta)$ appearing as anticipated along integer κ_θ. Fig. 21(a) and (b) are both symmetric relative to the x- and y-axis. A change of sign in κ_r indicates a spatial shift of 90°, and a change of sign in κ_θ marks a change in the rotation direction.

The simulated response of the rotating travelling wave along the rectangular membrane is shown using power-flow analysis to emphasize the rotation and direction of energy conveyance shown in Fig. 22 for κ_θ=2 and 3.

The rotating wave was experimentally tuned on the membrane device at 40 Hz using 32 actuators and measured along the mid membrane area (30×18 cm$^{2)}$. The measured results are depicted in Fig. 23(a) and (b) for κ_θ=3 and 2, respectively. The simulations and measured results show good compatibility with the desired response.

For links to animation movies of animated measured tuned responses available online, see the Appendix.

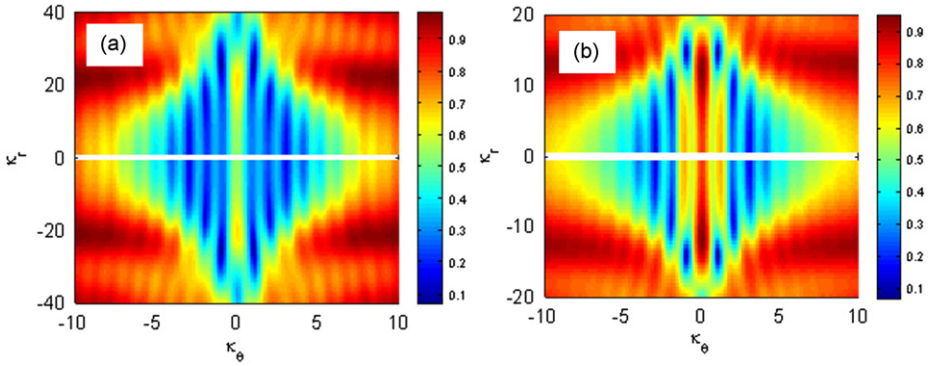

Fig. 21. Optimization mismatch surface of the spatial frequencies of a rotating travelling wave (Eq. (35))): (a) measured data at 40 Hz and (b) simulated data at 10 Hz.

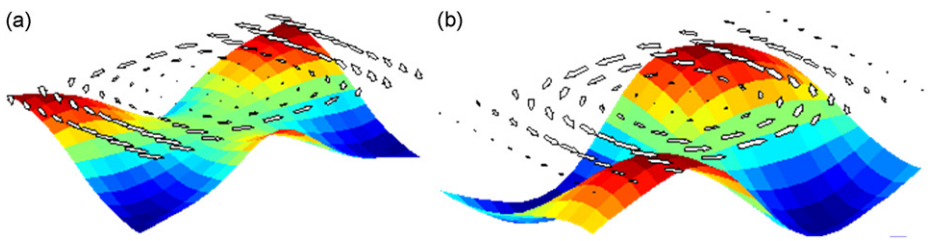

Fig. 22. Power-flow of simulated rotating travelling wave: (a) κ_θ=3 and (b) κ_θ=2.

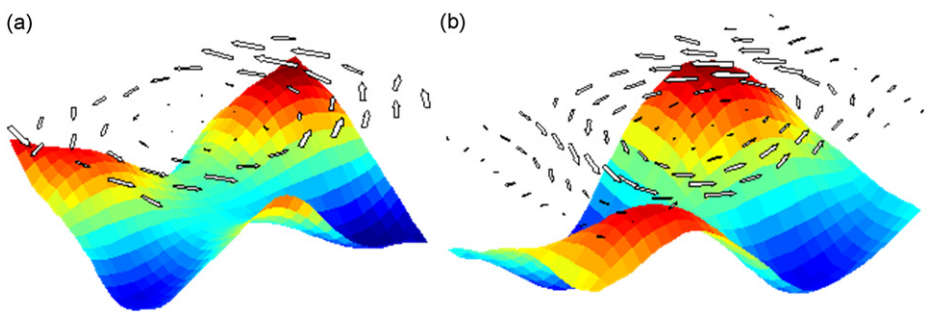

Fig. 23. Power-flow of measured rotating travelling wave: (a) κ_θ=3, (b) κ_θ=2 (40 Hz, 32 actuators, mid-membrane tuned and measured).

4. Conclusions

The presented numerical and experimental results indicate that the proposed tuning method has several advantages over other vibration tuning methods. Analytical force distribution calculation, for example, is highly dependent upon system parameters (tension, mass density, etc.), and is confined to simple geometries and boundary conditions. However, the proposed method requires little or even no previous knowledge of the system at hand prior to tuning. Moreover, dual- or multimode excitation, as a method to produce travelling waves, produces suboptimal results. These often combine vibration modes with slightly different wavelengths thus producing a standing wave component accompanying the travelling part. However, the presented non-modal method automatically detects and excites the required modes of vibration comprising the desired response, thus resulting in nearly pure travelling waves at the tuned area, however with somewhat lower amplitudes.

The proposed method is also capable of generating a desired response in the presence of nonlinear, undesired, sub- or super-harmonics. As shown, by dictating zero amplitude oscillation for unwanted frequencies, the algorithm drives energy into the system to actively decay these parasitic oscillations. Convergence by small perturbations allows the algorithm to achieve the desired response in mild nonlinear vibration regimes, such as in the proximity of natural frequencies, where amplitudes tend to rise. This capability is important in composing the response of a series incorporating several frequencies, as in the case of a triangular travelling wave, where all the terms should be in phase and the amplitudes ratios are predetermined.

The proposed tuning method was successfully applied to tuning vibration patterns that are not the well-known solution of the wave equation. Rotating vortexes as well as translatory travelling waves were realized numerically and experimentally on the same structure. The presented method automatically finds the combination of forces to yield the closest response possible to the desired one.

This paper has presented new techniques for linearity assessment. The analysis is based on comparing the structure of the measured system model matrix with the theoretical linear block structure (Eq. (9)). Nonlinear effects such as sub- or super-harmonics are detected by the cross-coupling blocks of the multi-frequency model (Eq. (19)).

This paper has proposed wavelength optimization methods that minimize the anticipated mismatch between the desired responses for one- and two-dimensional structures. These methods are used to optimize the measured response.

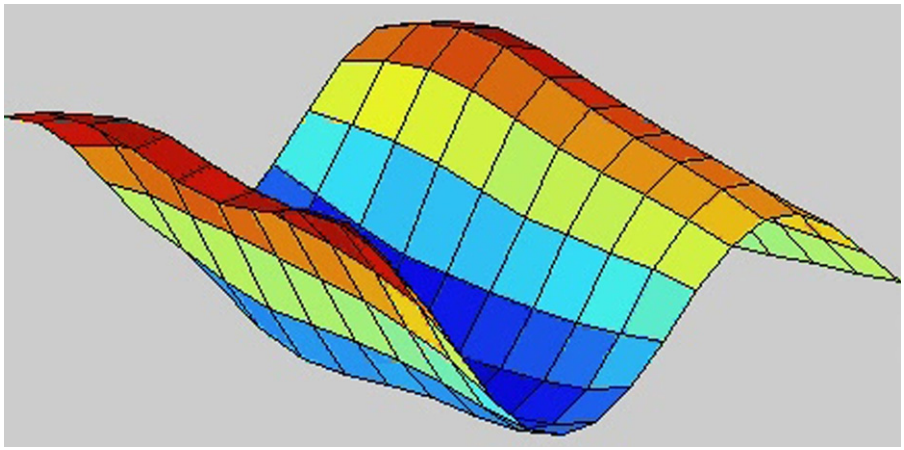

Movie 1. Animated measurements of a travelling wave propagating at an angle $\theta=0^\circ$. Tuning and measuring are conducted on the same 30×18 cm^2 membrane section.

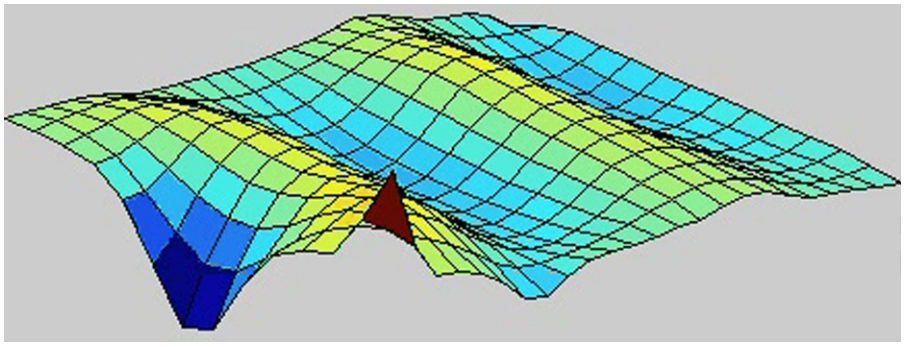

Movie 2. Animated measurements of a travelling wave propagating at an angle $\theta=0^\circ$ on a 46×26 cm^2 membrane section. Tuning was conducted on the mid 30×18 cm^2 section.

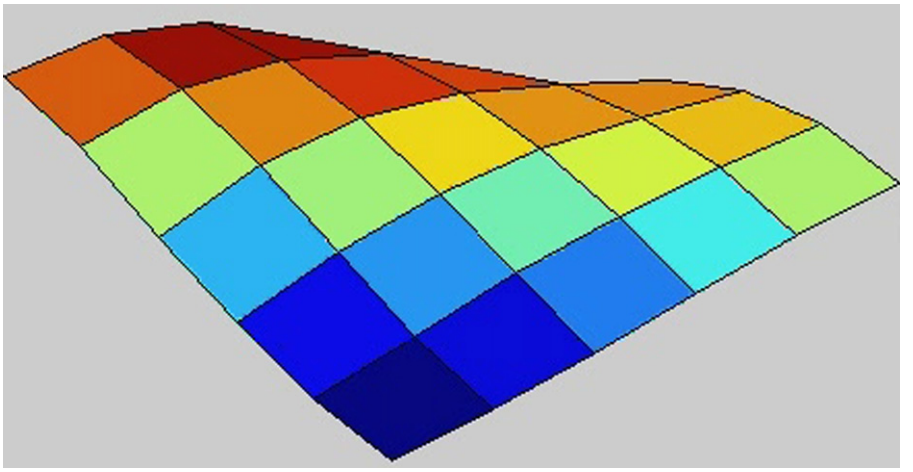

Movie 3. Animated measurements of a travelling wave propagating at an angle $\theta = -45^{o}$. Tuning and measuring are conducted on the same 10×10 cm^2 membrane section.

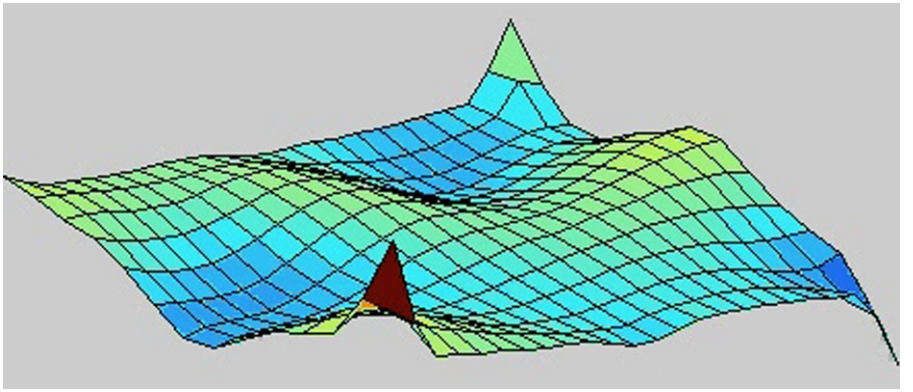

Movie 4. Animated measurements of a travelling wave propagating at an angle $\theta = -45^{\circ}$ on a 46×26 cm^2 section. Tuning was conducted on the mid 30×18 cm^2 section.

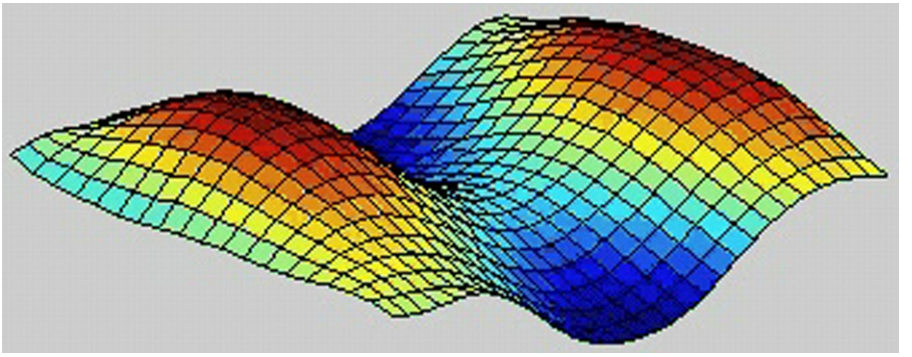

Movie 5. Animated measurements of a tuned vortex with an angular wavenumber $\kappa_{\theta}=2$. Tuning and measuring are conducted on the same 30×18 cm^2 membrane section.

Acknowledgements

This work has been partially supported by the Israeli Science Foundation, Grant no. 574/04.

The authors would like to acknowledge the contributions of Dr. Ran Gabai, Mr. Harel Plat, and Mr. Hadar Raz for sharing their knowledge and enthusiasm with us.

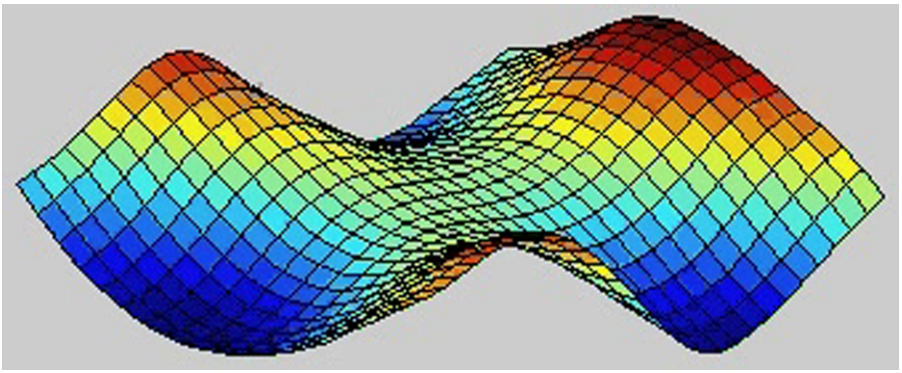

Movie 6. Animated measurements of a vortex with an angular wavenumber κ_θ=3. Tuning and measuring are conducted on the same $30 \times 18\ \mathrm{cm}^2$ membrane section.

Appendix: Links to animations of experimental measurements

The following are the supplementary data to this article:
Movies 1 to 6.

References

[1] A. Minikes, I. Bucher, Non-contacting lateral transportation using gas squeeze film generated by flexural travelling waves-numerical analysis, *Journal of the Acoustical Society of America* 113 (2003) 2464–2473.
[2] A. Minikes, R. Gabay, I. Bucher, M. Feldman, On the sensing and tuning of progressive structural vibration waves, *IEEE Transactions on Ultrasonics, Ferroelectrics, and Frequency Control* 52 (9) (2005) 1565–1575.
[3] Y. Chen, S. Ma, B. Li Wang, Analysis of travelling wave locomotion of snake robot, *Proceedings of the 2003 IEEE, International Conference on Robotics, Intelligent Systems, and Signal Processing*, Changsha, China, October 2003.
[4] L.E. Becker, S.A. Koehler, H.A. Stone, On self-propulsion of micro-machines at low Reynolds number: Purcell's three-link swimmer, *Journal of Fluid Mechanics* 490 (2003) 15–35.
[5] W.J. O'Connor, D. Lang, Position control of flexible robot arms using mechanical waves, *ASME Journal of Dynamics Systems, Measurement and Control* 120 (3) (1998) 334–339.
[6] H. Iwamoto, N. Tanaka, Adaptive feed-forward control of flexural waves propagating in a beam using smart sensors, *Smart Materials and Structures* 14 (6) (2005) 1369–1376.
[7] H. Iwamoto, N. Tanaka, Feedforward control of flexural waves propagating in a rectangular panel, *Journal of Sound and Vibration* 324 (1-2) (2009) 1–25.
[8] M. Kuribayashi, S. Ueha, E. Mori, Excitation conditions of flexural travelling waves for a reversible ultrasonic linear motor, *Journal of the Acoustical Society of America* 77 (1985) 1431–1435.
[9] S. Ueha, Y. Tomikawa, with contributions from M. Kurosawa and N. Nakamura, *Ultrasonic Motors: Theory and Applications*, Clarendon Press, Oxford, 1993.
[10] J.F. Manceau, S. Biwersi, F. Bastin, On the generation and identification of travelling waves in non-circular structures—application to innovative piezoelectric motors, *Smart Material Structures* 7 (1997) 337–344.
[11] J.F. Manceau, F. Bastin, Production of quasi-travelling wave in a silicon rectangular plate using single phase drive, *Transactions on Ultrasonic, Ferroelectric, and Frequency Control* 42 (1) (1995).
[12] R. Gabai, I. Bucher, Spatial and temporal excitation to generate travelling waves in structures, *Journal of Applied Mechanics* 77 (2) (2010) 021010.
[13] T.H. Vose, P. Umbanhowar, K.M. Lynch, Friction-induced velocity fields for point parts sliding on a rigid oscillated plate, *International Journal of Robotics Research* 28 (8) (2009) 1020–1039.
[14] C. Fink, S. Ergu'n, D. Kralisch, U. Remmers, J. Weil, T. Eschenhagen, Chronic stretch of engineered heart tissue induces hypertrophy and functional improvement, *The FASEB Journal* 14 (2000) 669–679.
[15] N. Tanaka, S.D. Snyder, Y. Kikushima, M. Kuroda, Vortex structural power flow in a thin plate and the influence on the acoustic field, *Journal of the Acoustical Society of America* 96 (3) (1994) 1563–1574.
[16] I. Bucher, Exact adjustment of dynamic forces in presence of non linear feedback and singularity—theory and algorithms, *Journal of Sound and Vibration* 218 (1) (1998) 1–27.
[17] G. Strang, K. Borre, *Linear Algebra, Geodesy and GPS*, Wellesley-Cambridge Press, MA, USA, 1997.
[18] A. Ben-Israel, Thomas N.E. Greville, *Generalized Inverses: Theory and Applications*, Springer, New York, 2003.
[19] B. Noble, J.W. Daniel, *Applied Linear Algebra*, 3rd ed., Prentice-Hall International, Englewood Cliffs, NJ, 1988.
[20] I. Bucher, Estimating the ratio between travelling and standing vibration waves under non-stationary conditions, *Journal of Sound and Vibration* 270 (2004) 341–349.
[21] R. Gabai, Generating, Sensing and Controlling Progressive Waves in One and Two Dimensions, a Theoretical and Experimental Study, PhD Thesis, Technion-Isreali Institute of Technology, 2009.
[22] J.D. Achenbach, *Wave Propagation in Elastic Solids*, NHPC (1973).
[23] R. Gabai, E. Setter, H. Plat, I. Bucher, Power flow control and travelling waves of vibration, the optimal force distribution, *ICEDyn International Conference on Structural Engineering Dynamics*, June 2009, Ericeria, Portugal.
[24] M.J. Brennan, S.J. Elliott, R.J. Pinnington, Active control of flexural waves using power as a controlling parameter, *Proceedings of the Fifth International Conference on Recent Advances in Structural Dynamics*, Southampton, UK, 2, 1994, pp. 973–982.